Thermodynamic Assessment of a Supercritical CO_2 Geothermal Well coupled with an R1234ze(E) ORC

George Antoneas[a], Tryfon C. Roumpedakis[a,]*, Andreas Nikoglou[b], Irene Koronaki[a] and Sotirios Karellas[b]

[a] Laboratory of Applied Thermodynamics, National Technical University of Athens (NTUA), Greece,
troumpedak@mail.ntua.gr
[b] Laboratory of Thermal Processes, National Technical University of Athens (NTUA), Greece,
anikog@mail.ntua.gr

Abstract:

Geological formations hold significant potential for simultaneous carbon dioxide (CO_2) storage and energy extraction through CO_2 Plume Geothermal (CPG) systems. However, accurately evaluating their viability requires coupling subsurface heat-transfer dynamics with surface power conversion performance. This study conducts a thermodynamic assessment of a supercritical CO_2 geothermal well integrated with a subcritical Organic Rankine Cycle (ORC) utilizing the low-GWP fluid R1234ze(E). Using an integrated framework, a numerical reservoir and wellbore model are coupled with an hourly off-design ORC simulation to evaluate seasonal and long-term system behavior. The annual assessment demonstrates that the system can operate for 6616 hours per year, achieving a maximum net power output of 1.42 MW and generating 6422 MWh of net electricity. The system achieves a mean net thermal efficiency of 8.84%, which is strongly governed by seasonal dispatch profiles and ambient-dependent condensation limits. Furthermore, a 30-year long-term analysis reveals that while progressive reservoir depletion lowers the produced CO_2 temperature and shifts thermal efficiencies downward, the hybrid CPG-ORC system maintains acceptable performance and delivers meaningful electricity production throughout its operational lifespan.

Keywords:

Supercritical CO_2; Geothermal energy; Organic Rankine cycle; CO_2 Plume Geothermal

1. Introduction

Over the last decade the green energy transition has shifted considerably the share of renewable electricity; at the same time, a key challenge of the low-carbon energy systems remains the operation in a stable and dispatchable manner. In this context, geothermal energy poses a highly attractive option, being able to provide continuous power output with a relatively small environmental footprint and high availability compared to intermittent renewable sources [1]. However, the effective utilization of geothermal resources depends strongly on the thermodynamic characteristics of the geothermal fluid and the suitability of the surface system. Among various geothermal concepts, systems utilizing carbon dioxide as the subsurface working fluid have received growing attention over the last years. Under supercritical conditions, CO_2 offers favorable thermophysical properties, including high density, high thermal expansivity, and low kinematic viscosity, making it an ideal medium for heat extraction and wellbore transport [2].

Supercritical CO_2 systems offer operational advantages over conventional water-brine systems, contributing to enhanced energy recovery [3]. Recent studies emphasize the strategic value of CO_2 Plume Geothermal (CPG) systems in addressing energy challenges, highlighting CPG systems' adaptability for decentralized, sustainable power generation [4,5]. Despite this subsurface CPG potential, the thermal energy delivered at the wellhead must be efficiently converted into electricity. For low to medium temperature wellheads direct expansion of CO_2 is considered unfavourable from a thermodynamic viewpoint. For such temperature levels, Organic Rankine Cycle (ORC) is a practical, mature solution that significantly supports sustainability in low grade energy conversion, while offering flexibility in operating pressures, heat-exchanger design, and working-fluid selection [6]. Organic fluid selection is critical for the ORC thermal efficiency as well as the geothermal heat source thermal matching. The modern regulatory landscape also necessitates the use of ultra-low Global Warming Potential (GWP) fluids; thus, employing hydrofluoroolefins (HFOs) like R1234ze(E) ensures the environmental sustainability of the cycle while maintaining high thermal and exergy efficiencies [7,8]. Key challenge in the thermodynamic analysis of such systems is the integration of subsurface and surface models. In many thermodynamic assessments, geothermal source conditions are prescribed statically without detailed consideration of wellbore heat-transfer dynamics, which imposes large uncertainties in the system's predicted performance [9]. This simplification limits the validity of such analyses, as ORC performance is highly sensitive to the temperature level, heat capacity rate, and cooling profile of the geothermal stream delivered to the surface. Therefore, a more rigorous approach requires coupling physics-based geothermal well modelling with a dedicated thermodynamic model of the ORC to better simulate the interaction of the two systems.

To bridge this gap, the present study conducts a thermodynamic assessment of a supercritical CO_2 geothermal system coupled to a large scale ORC, operating with R1234ze(E), under an integrated modelling approach. The geothermal well is modelled in COMSOL to accurately predict the thermodynamic conditions of the produced CO_2 at the surface, while a dedicated Python-based model simulates the ORC performance. In this configuration, supercritical CO_2 arriving at the surface equipment at approximately 130 °C serves solely as the heat source in the evaporator. The ORC is designed with an evaporation temperature of 100 °C and a target superheating temperature of 5 K. The primary objective of this study is to quantify the thermodynamic viability of the investigated configuration. By focusing on the evaporator heat-load distribution and thermal matching, the results of this study aim to link realistic off-design wellhead conditions with common power generation performance indicators, providing critical guidance for the design of hybrid geothermal-ORC systems.

2. GEOTHERMAL RESERVOIR PROPERTIES

For geothermal reservoir modelling purposes, we utilize geological formations that meet the petrophysical requirements of the Upper Jurassic Malm reservoir in the South German Molasse Basin, southern Germany. Reservoir properties were derived from outcrop analogue studies and production data from existing deep geothermal wells in the region. A critical distinction must be made between matrix properties, which characterize the tight carbonate rock fabric, and effective reservoir properties, which govern fluid flow through secondary porosity features including fractures and karstification [10]. This distinction is fundamental to CO_2-based geothermal system modelling, as reservoir-scale permeability enabling commercial flow rates is dominated by secondary porosity rather than the microporous matrix. In fractured reservoirs, dual-continuum modelling approaches have demonstrated that fracture permeability governs overall system performance in CO_2-based geothermal systems [11].

2.1. Reservoir Model Setup

The permeability and porosity values assigned to the model are selected to represent the bulk reservoir behaviour, integrating both matrix and secondary porosity contributions. For the effective properties, a permeability of 5×10^{-14} m² and a porosity of 10% are adopted. These values are derived from petrophysical data from the Upper Jurassic Malm reservoir in the South German Molasse Basin. Documented permeabilities range from 10^{-18} to 10^{-13} m², with higher values associated with specific lithofacies such as grainstones and dolomitized zones [12]. The selected permeability of 5×10^{-14} m² falls within this higher range, reflecting the influence of dolomitized or grain-dominated facies known to exhibit enhanced inter-crystalline porosity and improved matrix flow properties [13]. Regarding porosity, absolute porosities for the Higher Malm reservoir range from 1.6% to 16.2%, with an average of 7.3% [14]. Additional core measurements document effective porosities from 0.3% to 19.2% [10,15], while massive limestones typically exhibit porosities below 8%, with grainstones and dolomitized zones reaching up to 18% [10,12]. The selected porosity of 10% falls within these documented ranges and is consistent with values used in regional reservoir characterizations [16]. This value provides a realistic basis for evaluating the contribution of matrix properties relative to fracture-dominated flow in the dual-continuum model.

Based on these characteristics, a numerical model of a CO_2-based geothermal system is developed using a theoretical two-dimensional areal square geothermal reservoir representing a 0.81 km² (900 m × 900 m) map-view domain. This domain size is selected to balance computational efficiency with the need for a representative well configuration. A triplet geothermal exploitation scheme is implemented, consisting of two production wells and one injection well located at the centre of the domain, each with a diameter of 0.41 m. The distance between the central injection well and each production well is set at 636.4 m, positioning the production wells at opposite corners of the square domain. The system is assumed to be closed with respect to lateral boundaries, implying no heat or fluid exchange across the domain edges. The Upper Jurassic reservoir, which constitutes the key geothermal zone, ranges in thickness from 300 to 650 m [16] and contains warm fluid (65–130°C) hosted in fractured, karstified, and dolomitized carbonate rocks [17]. For the present model, a uniform reservoir thickness of 370 m is adopted, consistent with thickness values used in prior modelling studies of the Molasse Basin [18].

Model parameters are selected to reflect conditions beneath the Munich area, where three main operating geothermal facilities are located (Dürrnhaar, Kirchstockach, Sauerlach). Using a mean annual surface temperature of 8.2°C for Germany [17] and a regional geothermal gradient of 32°C/km [17], a well vertical depth of 3800 m is specified, yielding a bottom-hole temperature of approximately 130°C [19]. The initial reservoir pressure is set to 380 bar, corresponding to a hydrostatic pressure gradient of approximately 10 MPa/km at a depth of 3800 m. This pressure ensures that CO_2 remains in the supercritical state throughout the reservoir (critical point: 31°C, 73.8 bar), providing favourable mobility and heat capacity for geothermal extraction [20].

Regarding thermo-physical properties, grain density is set to 2650 kg/m³, falling within the range of 2590–2800 kg/m³ reported for outcrop samples. Thermal conductivity is set to 2 W/(m·K), representative of thick-bedded and platy limestones [13], and consistent with the range of 1.92–3.53 W/(m·K) reported for grain-dominated facies under saturated reservoir conditions [21]. Specific heat capacity is set to 1000 J/(kg·K), which lies within the overlapping range of 806–1227 J/(kg·K) and 711–1330 J/(kg·K) reported for matrix- and grain-dominated Malm carbonate facies, respectively, under saturated conditions at 150°C, based on the transfer model of Vosteen & Schellschmidt [22,23].

2.2. Porous Media Governing Equations

The numerical simulations are performed using COMSOL Multiphysics, coupling Darcy's Law for fluid flow with Heat Transfer in Porous Media. A time-dependent study is conducted to capture the transient behavior of the CO_2 plume and thermal front propagation. The continuity equation for fluid flow in a porous medium is given by:

$$\frac{\partial}{\partial t}\left(\varepsilon_p \rho\right) + \nabla \cdot (\rho u) = Q_m \tag{1}$$

where ε_p is the porosity, ρ is the fluid density, u is the Darcy velocity vector, and Q_m is a mass source/sink term representing injection and production wells. The Darcy velocity is governed by Darcy's law:

$$u = -\frac{\kappa}{\mu}\nabla p \tag{2}$$

where κ is the effective permeability of the porous medium, μ is the dynamic viscosity of CO_2, and p is the fluid pressure. The negative sign indicates flow from high to low pressure. The heat transfer equation in porous media is given by:

$$d_z\left(\rho C_p\right)_{eff}\frac{\partial T}{\partial t} + d_z\left(\rho c_p\right)u + \nabla T + \nabla \cdot q = d_z Q \tag{3}$$

where d_z is the reservoir thickness, c_p is the fluid specific heat capacity and T is the temperature. Conductive heat flux is described by Fourier’s law:

$$q = -d_z k_{eff} \nabla T \tag{4}$$

with k_{eff} being the effective thermal conductivity of the saturated porous medium. The term $\left(\rho C_p\right)_{eff}$ represents the effective volumetric heat capacity of the solid-fluid system, defined as:

$$\left(\rho C_p\right)_{eff} = \varepsilon_p \rho_f C_{p,f} + (1 - \varepsilon_p)\rho_s C_{p,s} \tag{5}$$

with subscripts f and s denote fluid and solid phases, respectively.

2.3. Wellbore Flow Model

The wellbore flow system is modelled using Python with CoolProp [24] as the fluid thermodynamic properties database, following the approach described by [25–27]. The pressure and temperature profiles within the injection and production wells are computed using a discretized wellbore model. Each well is divided into 20 m length segments, with properties evaluated iteratively along the flow path. For each segment, the total pressure change ΔP is calculated by considering both frictional losses and hydrostatic pressure variations:

$$\Delta P = \rho g \Delta z - \Delta P_{f,w} \tag{6}$$

where Δz is the segment length, and $\Delta P_{f,w}$ is the frictional pressure drop, expressed using the Darcy-Weisbach equation [28]:

$$\Delta P_{f,w} = f\frac{\Delta z \rho V^2}{2D} \tag{7}$$

The friction factor is determined by the following correlation [29]:

$$\frac{1}{\sqrt{f}} = -1.8\log\left[\left(\frac{\varepsilon}{3.7D}\right)^{1.11} + \frac{6.9}{Re}\right] \tag{8}$$

with ε representing the wellbore roughness. Heat transfer between the wellbore fluid and the surrounding formation is modeled using the [30] wellbore heat transmission approach. The temperature gradient along the well is given by:

$$\frac{dT}{dz} = -\frac{\pi D U_{total}}{\dot{m} C_p}\left(T_f - T_p\right) \tag{9}$$

$$\frac{1}{U_{total}} = \frac{1}{U} + \frac{D f(t_D)}{2k} \tag{10}$$

where T_f, T_p are the fluid and formation temperatures (K), respectively. The overall heat transfer coefficient U_{total} accounts for conductive resistance through wellbore materials, U, and transient heat transfer in the formation; $f(t_D)$ is the transient formation resistance dimensionless function [31], and k is the formation thermal conductivity. Additionally, the Joule-Thomson effect is incorporated to account for temperature changes resulting from pressure drops along the wellbore under adiabatic conditions [32].

3. ORC Thermodynamic Model

The ORC is modeled as a steady-state system in Python using R1234ze(E) as working fluid, with all thermophysical properties derived from CoolProp [24]. The simulation is divided into a design mode, in which the main component sizes are defined, and an hourly off-design mode, in which the cycle is solved under variable ambient conditions, requested power loads and geothermal-source availability.

At design conditions, the ORC is sized on the geothermal heat available from the prescribed CO_2 inlet temperature, the minimum CO_2 return temperature and the CO_2 mass-flow rate. The evaporation temperature is imposed from the source-side pinch point constraint, $T_{\mathrm{evap}} = T_{CO_2,\mathrm{PP}} - \Delta T_{PP}$, while the expander inlet temperature is defined by a fixed superheat, $T_{\mathrm{exp,in}} = T_{\mathrm{evap}} + \Delta T_{\mathrm{sh}}$. Fig. 1(a) shows the design-duty Q-T diagram of the evaporator with the imposed pinch-temperature constraint that defines the hot-side thermal matching. The condensing temperature is linked to the ambient condition through a fixed ACC approach point, $T_{\mathrm{cond}} = T_{\mathrm{amb}} + \Delta T_{\mathrm{app,ACC}}$. The ORC mass flow rate follows from the evaporator energy balance,

$$\dot{m}_{\mathrm{ORC}} = \frac{\dot{Q}_{\mathrm{in}}}{h(p_{\mathrm{evap}}, T_{\mathrm{exp,in}}) - h(p_{\mathrm{evap}}, T_{pump,out})}. \tag{11}$$

For the design mode, rather than prescribing a single design ambient state, the model scans the annual weather series and selects the hour that maximizes the predicted net ORC power. The expander is represented by polynomial performance maps. For a given inlet state and expansion ratio, r_p, the map returns the isentropic efficiency, volumetric efficiency, outlet enthalpy, rotational speed, and an estimate of the internal volume ratio, as shown in the example of Figure 1(b). During design, the built-in volume ratio is kept constant and the swept volume is iteratively adjusted until the nominal speed of 1800 rpm is matched. Net power is then obtained from the actual enthalpy drop across the expander reduced by the pump consumption,

$$P_{\mathrm{net}} = \dot{m}_{\mathrm{ORC}}\left(h_{\mathrm{exp,in}} - h_{\mathrm{exp,out}}\right) - P_{pump} \tag{12}$$

The heat exchangers are sized at design conditions using the LMTD method,

$$\dot{Q} = UA\Delta T_{\mathrm{lm}}. \tag{13}$$

A common shell and tube heat exchanger, acting as the ORC evaporator in power mode, is sized with typical estimated heat transfer coefficients in the range of 900-1000 W/m²K while the air-cooled condenser is sized with an typical heat transfer coefficients around 40-45 W/m²K.

In off-design operation, the hardware obtained at design conditions is kept fixed and only the operating point is updated hourly. Part-load operation is imposed by scaling the maximum available CO_2 mass flow rate with the dispatch fraction specified in the ORC load profile. The available geothermal heat is approximated as:

$$\dot{Q}_{\mathrm{geo,avail}} = \dot{m}_{\mathrm{CO_2,max}}\, c_{p,\mathrm{CO_2}}\left(T_{\mathrm{CO_2,in}} - T_{\mathrm{CO_2,out,min}}\right), \tag{14}$$

When the ORC is active, the expander inlet temperature is set from the hot pinch point restriction, similarly to the design mode and the superheating temperature is obtained from the estimated evaporation temperature considering the target design superheating and checking that no pinch point error occurs; the condensing temperature remains coupled to ambient air through the fixed ACC approach. If $T_{\mathrm{evap}} \leq T_{\mathrm{cond}} + 20$, the operating point is rejected as thermodynamically infeasible.

Off-design heat-exchanger performance is evaluated through ε–NTU method. Considering a typical counterflow heat exchanger without mixing for the ACC in eq.(17) and a shell and tube with 2-passes version for the evaporator in eq.(18) [33],

$$\mathrm{NTU} = \frac{UA}{C_{\mathrm{min}}} \tag{15}$$

$$C_r = \frac{C_{\mathrm{min}}}{C_{\mathrm{max}}}, \tag{16}$$

$$\varepsilon_{hex,ACC} = 1 - \exp\left\{\frac{1}{C_r}\, NTU^{0.22}\left[exp\left(-C_r\, NTU^{0.78}\right) - 1\right]\right\} \tag{17}$$

$$\varepsilon_{hex,evap} = 2\left[1 + C_r + \frac{1 + exp\left(-NTU\sqrt{1+C_r^2}\right)}{1 - exp\left(-NTU\sqrt{1+C_r^2}\right)}\sqrt{1 + C_r^2}\right]^{-1} \tag{18}$$

The feed pump is modeled with a polynomial curve fitted isentropic efficiency, and the ORC mass flow rate is recalculated from the evaporator duty and the enthalpy rise between pump outlet and expander inlet. The expander is then solved with the same polynomial map used during design mode, but now with fixed swept volume and varying pressure ratio and inlet state. The hourly ORC outputs reported by the current implementation are the evaporator heat input, net expander power, net thermal efficiency, and condenser heat rejection. Accordingly, the net cycle performance is described by:

$$\eta_{\text{net}} = \frac{P_{\text{net}}}{\dot{Q}_{\text{in}}}. \qquad (19)$$

The condenser rejection load is first estimated from the ORC energy balance and then limited by the fixed ACC conductance through a simplified effectiveness–NTU relation. Within these assumptions, the model provides a computationally efficient framework for annual ORC performance prediction under variable source and ambient conditions.

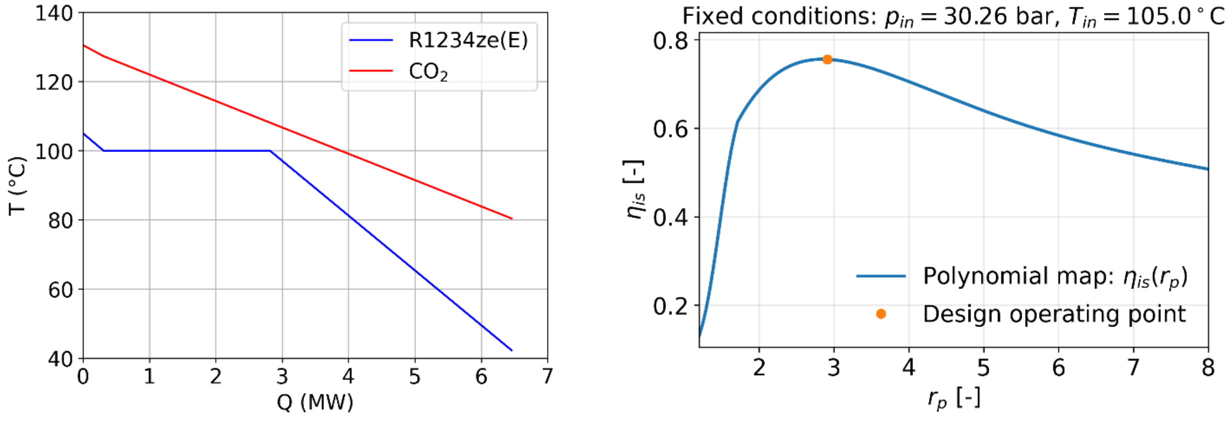

(a) *(b)*

Figure. 1. *(a) Q-T diagram of each ORC module in design 6.5MW well thermal input (b) Turbine isentropic efficiency as a function of expansion pressure ratio*

4. Results

4.1. Subsurface behaviour

To assess the influence of domain size on long-term thermal performance, five square reservoir configurations ranging from 0.36 km² to 1 km² are evaluated. The injection-to-production well distance in each case is determined by the domain geometry, as the injection well is fixed at the center and the two production wells are positioned at opposite corners of the square domain, as described in Section 2.1. The computational domain is extended slightly beyond the nominal reservoir area to avoid placing the production wells exactly at the domain boundary, ensuring numerical stability at the well nodes without affecting the effective well spacing or the reservoir flow geometry.

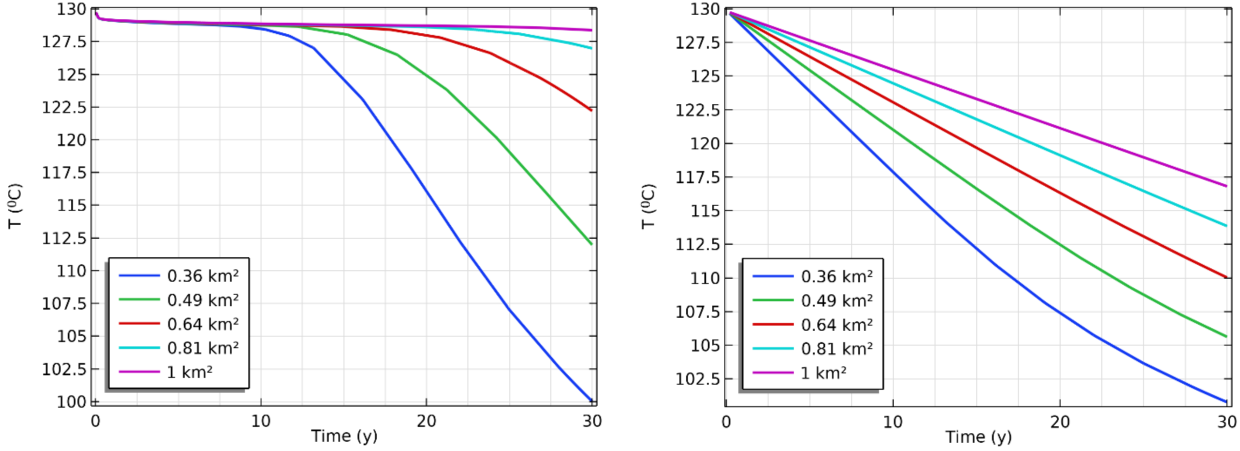

(a) *(b)*

Figure. 2. *(a) Production well temperature as a function of time for five reservoir domain sizes ranging from 0.36 km² to 1 km², illustrating the effect of injection-to-production well spacing on thermal breakthrough over a 30-year operational period. (b) Domain-averaged reservoir temperature decline as a function of time for the same domain configurations, reflecting the overall thermal depletion of the reservoir under constant mass flow rate injection.*

Figure 2(a) presents the produced fluid temperature at the production wells over the 30-year simulation period. Smaller domains exhibit pronounced thermal breakthrough, with the 0.36 km² case reaching approximately 100°C by year 30, while the 1 km² case retains a production temperature close to the initial reservoir value of 130°C. The 0.81 km² configuration shows a decline of approximately 2°C over the full simulation period, representing a favorable balance between reservoir utilization and thermal sustainability over the design lifetime. Figure 2(b) presents the domain-averaged temperature decline across all cases. Smaller reservoirs experience steeper cooling due to the limited thermal mass available relative to the extraction rate, whereas larger domains maintain higher average temperatures throughout operation. In the 0.81 km² case, the cold front remains concentrated in the vicinity of the central injection well due to the symmetric dipole flow pattern imposed by the triplet configuration, while the two production wells remain largely thermally unaffected over the simulation period (Figure 3). This spatial decoupling between injection and production zones is a key advantage of the triplet arrangement, as it delays thermal breakthrough and preserves production temperature over the operational lifetime of the system.

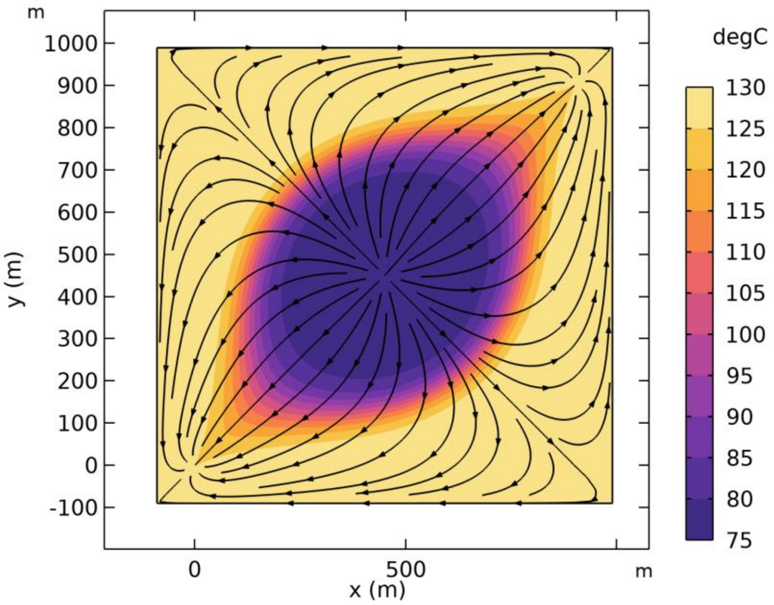

Figure. 3. *Two-dimensional temperature distribution and fluid flow streamlines within the 0.81 km² reservoir domain at t = 30 years, illustrating the symmetric thermal plume developed under the triplet well configuration with central injection and corner production wells.*

4.2. ORC performance

The annual ORC assessment was carried out with the hardware fixed at the design point and with hourly variation imposed only through the supervisory load request and the ambient sink conditions. In the present ORC-only scenario, the geothermal source supplied to the surface model was kept at 130 °C, with a minimum return temperature of 80 °C and a target superheating of 5 K. Under these assumptions, the annual performance is governed primarily by two external drivers: the requested ORC load fraction and the ambient temperature acting on the air-cooled condenser. Figure 4(a) presents the requested ORC load profile for a full year operation. The dispatch logic imposes full-load operation during winter and gradually transitions to reduced operation during the warm season, where normally wind and solar energy dominate the electricity mix and thus limited penetration is needed from the proposed system. In particular, summer daytime operation is suppressed, while summer night-time operation is maintained at 50% of nominal load. The transition between winter and summer operation is smoothed through the cosine seasonal weighting implemented in the control profile, which avoids abrupt changes in the requested load, while a minimum load fraction of 30% was assumed below which ORC was shutting down.

Figure 4(b) shows the ambient temperature profile used in the off-design analysis. Since the ORC condensing temperature is coupled to the ambient condition through the fixed ACC approach, colder periods improve the condenser-side heat rejection and thus increase the effective expansion ratio, whereas warmer periods shift the cycle toward higher condensation temperatures/pressures and reduced thermodynamic performance.

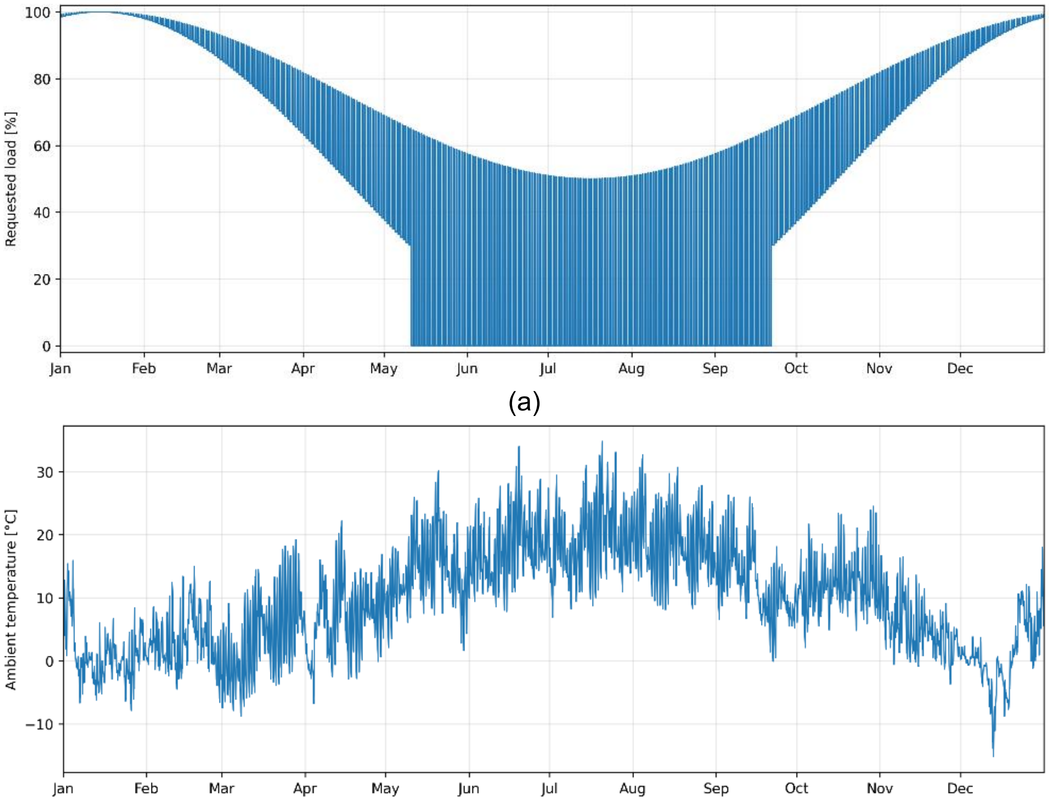

(a)

(b)

Figure. 4. *(a) Requested load profile (b) Ambient conditions*

The resulting annual ORC response follows the aforementioned boundary conditions closely. The model predicts 6616 h of applied ORC operation over the year, with a maximum net power output of 1.42 MW and an annual net electricity generation of 6422 MWh. Over the annual operation, the mean net thermal efficiency was around 8.84%, a value that is at the same levels with conventional exhaust gas driven ORC systems with similar heat source temperature levels [34,35]. These results indicate that the integrated geothermal-ORC system is utilized efficiently as a seasonally modulated power unit, delivering its highest output during cold periods and reduced output during summer, when the sink temperature penalizes condensation and the dispatch profile intentionally limits the requested load.

Figure 5 shows the seasonal coupling between power production and ORC thermal efficiency during the first year of operation (no depletion of the reservoir temperature). Higher output and efficiency are observed during cold periods, when the lower ambient temperature improves condenser operation and supports more favorable expansion conditions, whereas both quantities decline during warmer periods because of the increased condensation temperature and the reduced dispatched load. This behavior confirms that the annual ORC response is controlled jointly by the seasonal operating schedule and the ambient-dependent limitations of the ACC.

Figure 6 extends the analysis to the long-term operation of the hybrid system, presenting the yearly span of ORC net thermal efficiency over a 30-year period, together with the corresponding produced CO_2 temperature. As reservoir depletion progresses, the temperature of the produced fluid gradually decreases, reducing the effective temperature level of the heat source available to the ORC. This leads to a systematic downward shift of the annual efficiency, with the maximum, average, and minimum yearly efficiencies all decreasing over time at a different rate. As shown in Figure 6, during the first years of operation, the ORC maintains a comparatively higher and broader efficiency span, whereas in later years both the maximum reported efficiency and the lower operating bound move to smaller values, showcasing how the long-term geothermal depletion directly impacts the thermodynamic quality of the heat source and consequently the ORC performance.

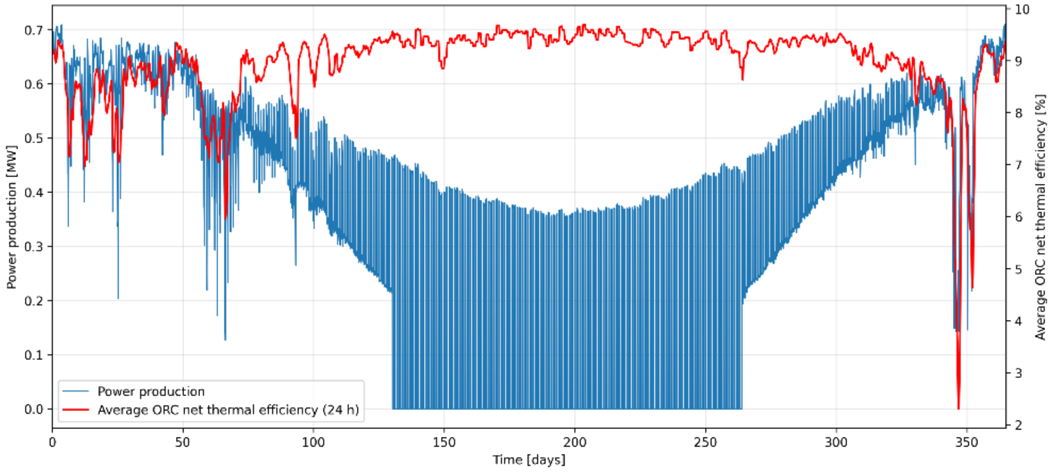

Figure. 5. *Power production and average ORC net thermal efficiency for the first year of operation*

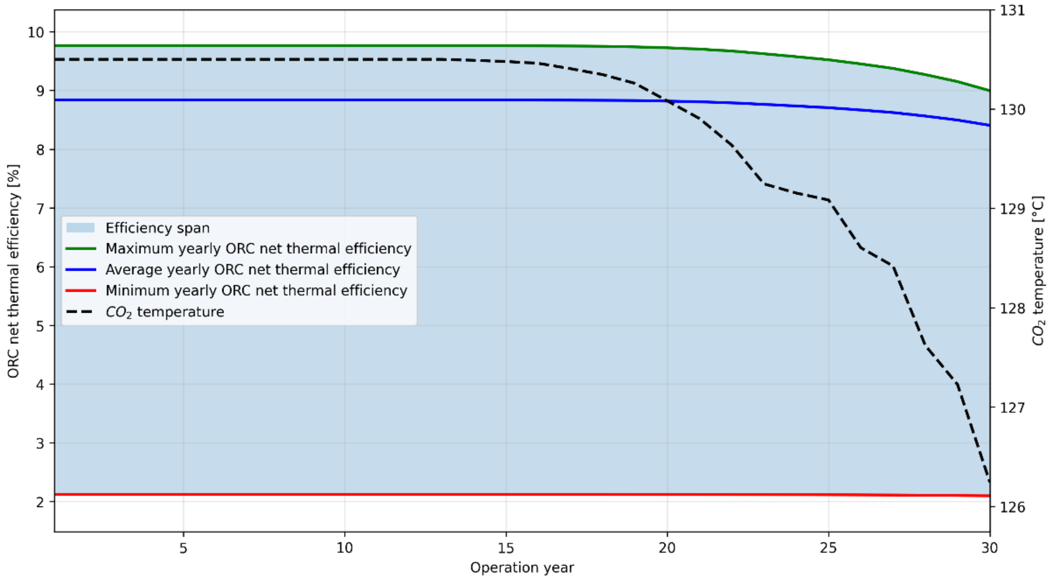

Figure. 6. *Predicted span of ORC net thermal efficiency over 30 years of operation together with the produced CO_2 temperature.*

5. Conclusions

This study investigated the thermodynamic feasibility of coupling a supercritical CO_2 geothermal well with a subcritical ORC operating with R1234ze(E), using an integrated modelling framework that combines reservoir and wellbore prediction with detailed ORC simulations. The key conclusions of the study are summarized below:

- the ORC annual assessment showed that the system can operate for 6616 h per year, reaching a maximum net power output of 1.42 MW and an annual net electricity generation of 6422 MWh.
- the mean net thermal efficiency was approximately 8.84%, which is within the expected range for ORC systems driven by medium-temperature heat sources.
- The first-year off-design results demonstrated that ORC performance is strongly governed by the combined effect of seasonal dispatch and ambient-dependent condensation.
- The long-term analysis over 30 years of operation showed that reservoir depletion progressively lowers the produced CO_2 temperature and causes a downward shift in the maximum, average, and minimum yearly ORC net thermal efficiencies.
- Despite the long-term depletion of the geothermal source, the results show that the proposed concept can deliver meaningful annual electricity production and maintain acceptable ORC performance under realistic seasonal and long-term operating conditions.

Acknowledgments

The first author would like to thank the Special Account for Research Funding (ELKE) of the National Technical University of Athens (NTUA) for its financial support during his doctoral studies.

Nomenclature

A	heat-transfer area, m²
c_p	specific heat capacity, J/(kg·K)
d	well diameter, m
f	friction factor, –
g	gravitational acceleration, m/s²
H	reservoir thickness, m
h	specific enthalpy, J/kg
k	effective permeability, m²
L	segment length, m
$\dot{m}$	mass flow rate, kg/s
NTU	number of transfer units, –
p	pressure, Pa
P	power, W
$\dot{Q}$	heat duty, W
Re	Reynolds number, –
r_p	pressure ratio, –
T	temperature, K
u	Darcy velocity, m/s
U	overall heat transfer coefficient, W/(m²·K)
v	fluid velocity, m/s

Greek symbols

ΔP	total pressure change, Pa
$\Delta P_{f,w}$	frictional pressure drop, Pa
ϵ	wellbore roughness, m
ε_{hex}	heat exchanger effectiveness,-
η	thermal efficiency, -
λ	effective thermal conductivity, W/(m·K)
μ	dynamic viscosity, Pa·s
ϕ	porosity, –
ρ	fluid density, kg/m³

Subscripts and superscripts

ACC	air cooled condenser
amb	ambient
app	approach
cond	condensing / condenser
eff	effective
evap	evaporation / evaporator
exp	expander
f	fluid
in	inlet
outoutlet	
p	formation
PP	pinch point
pump	pump

s	solid
sh	superheating / superheater

References

[1] Heberle F, Schifflechner C, Brüggemann D. Life cycle assessment of Organic Rankine Cycles for geothermal power generation considering low-GWP working fluids. Geothermics 2016;64:392–400. https://doi.org/10.1016/j.geothermics.2016.06.010.

[2] Cong L, Lu S, Jiang P, et al. Research Progress on CO2 as Geothermal Working Fluid: A Review. Energies 2024;17. https://doi.org/10.3390/en17215415.

[3] Evangeline SI, Darwin S. The role of carbon dioxide in enhancing geothermal energy: A review of current developments and future potential. Renewable and Sustainable Energy Reviews 2025;214:115525. https://doi.org/10.1016/j.rser.2025.115525.

[4] Schifflechner C, de Reus J, Schuster S, et al. Paving the way for CO2-Plume Geothermal (CPG) systems: A perspective on the CO2 surface equipment. Energy 2024;305:132258. https://doi.org/10.1016/j.energy.2024.132258.

[5] Antoneas G, Koronaki I. Geothermal Solutions for Urban Energy Challenges: A Focus on CO2 Plume Geothermal Systems. Energies 2024;17. https://doi.org/10.3390/en17020294.

[6] Roumpedakis TC, Fostieris N, Braimakis K, et al. Techno-Economic Optimization of Medium Temperature Solar-Driven Subcritical Organic Rankine Cycle. Thermo 2021;1:77–105. https://doi.org/10.3390/thermo1010007.

[7] Sun E, Sun Y, Feng S, et al. Thermodynamic study of organic Rankine cycle based on extraction steam compression regeneration in the supercritical state. Energy Conversion and Management 2023;293:117546. https://doi.org/10.1016/j.enconman.2023.117546.

[8] Dawo F, Fleischmann J, Kaufmann F, et al. R1224yd(Z), R1233zd(E) and R1336mzz(Z) as replacements for R245fa: Experimental performance, interaction with lubricants and environmental impact. Applied Energy 2021;288:116661. https://doi.org/10.1016/j.apenergy.2021.116661.

[9] Tagliaferri M, Gładysz P, Ungar P, et al. Techno-Economic Assessment of the Supercritical Carbon Dioxide Enhanced Geothermal Systems. Sustainability 2022;14. https://doi.org/10.3390/su142416580.

[10] Bohnsack D, Potten M, Pfrang D, et al. Porosity–permeability relationship derived from Upper Jurassic carbonate rock cores to assess the regional hydraulic matrix properties of the Malm reservoir in the South German Molasse Basin. Geotherm Energy 2020;8:12. https://doi.org/10.1186/s40517-020-00166-9.

[11] Chen M, Al-Alawi A, Reza Nikoo M, et al. Sensitivity analysis of a dual-continuum model system for integrated CO2 sequestration and geothermal extraction in a fractured reservoir. Sustainable Energy Technologies and Assessments 2024;72:104053. https://doi.org/10.1016/j.seta.2024.104053.

[12] Homuth S, Götz AE, Sass I. Lithofacies and depth dependency of thermo- and petrophysical rock parameters of the Upper Jurassic geothermal carbonate reservoirs of the Molasse Basin. Zdgg 2014;165:469–86. https://doi.org/10.1127/1860-1804/2014/0074.

[13] Homuth S, Götz AE, Sass I. Reservoir characterization of the Upper Jurassic geothermal target formations (Molasse Basin, Germany): role of thermofacies as exploration tool. Geoth Energ Sci 2015;3:41–9. https://doi.org/10.5194/gtes-3-41-2015.

[14] Dussel M, Lüschen E, Thomas R, et al. Forecast for thermal water use from Upper Jurassic carbonates in the Munich region (South German Molasse Basin). Geothermics 2016;60:13–30. https://doi.org/10.1016/j.geothermics.2015.10.010.

[15] Freitag S, Klaver J, Malai IS, et al. Petrophysical characterization, BIB-SEM imaging, and permeability models of tight carbonates from the Upper Jurassic (Malm ß), SE Germany. Geotherm Energy 2022;10:30. https://doi.org/10.1186/s40517-022-00239-x.

[16] Mraz E. Reservoir characterization to improve exploration concepts of the Upper Jurassic in the southern Bavarian Molasse Basin. Technische Universität München, 2019.

[17] Agemar T, Weber J, Schulz R. Deep Geothermal Energy Production in Germany. Energies 2014;7:4397–416. https://doi.org/10.3390/en7074397.

[18] Lentsch D, Savvatis A, Hofstätter H, et al. Potential of Multilateral Wells for Geothermal Projects in the South German Molasse Basin. Proceedings World Geothermal Congress 2020+1, Reykjavik, Iceland: 2021.

[19] Agemar T, Alten J-A, Ganz B, et al. The Geothermal Information System for Germany – GeotIS. Zdgg 2014;165:129–44. https://doi.org/10.1127/1860-1804/2014/0060.

[20] Randolph JB, Saar MO. Combining geothermal energy capture with geologic carbon dioxide sequestration. Geophys Res Lett 2011;38:L10401. https://doi.org/10.1029/2011GL047265.

[21] Homuth S, Sass I. Outcrop Analogue Vs. Reservoir Data: Characteristics and Controlling Factors of Physical Properties of the Upper Jurassic Geothermal Carbonate Reservoirs of the Molasse Basin, Germany n.d.

[22] Homuth S, Sass I. Outcrop Analogue Vs. Reservoir Data: Characteristics and Controlling Factors of Physical Properties of the Upper Jurassic Geothermal Carbonate Reservoirs of the Molasse Basin, Germany, 2014.

[23] Vosteen H-D, Schellschmidt R. Influence of temperature on thermal conductivity, thermal capacity and thermal diffusivity for different types of rock. Physics and Chemistry of the Earth, Parts A/B/C 2003;28:499–509. https://doi.org/10.1016/S1474-7065(03)00069-X.

[24] Bell IH, Wronski J, Quoilin S, et al. Pure and Pseudo-pure Fluid Thermophysical Property Evaluation and the Open-Source Thermophysical Property Library CoolProp. Ind Eng Chem Res 2014;53:2498–508. https://doi.org/10.1021/ie4033999.

[25] Adams B, Ogland-Hand J, M. Bielicki J, et al. Estimating the Geothermal Electricity Generation Potential of Sedimentary Basins Using genGEO (The Generalizable GEOthermal Techno-Economic Simulator). Chemistry; 2021. https://doi.org/10.26434/chemrxiv.13514440.v1.

[26] Atrens AD, Gurgenci H, Rudolph V. Electricity generation using a carbon-dioxide thermosiphon. Geothermics 2010;39:161–9. https://doi.org/10.1016/j.geothermics.2010.03.001.

[27] Marcolini M, Battistelli A. Modeling of wellbore flow within geothermal reservoir simulations at field scale. Proc. TOUGH Symposium 2012, Berkeley, CA: 2012.

[28] Brown GO. The History of the Darcy-Weisbach Equation for Pipe Flow Resistance. Environmental and Water Resources History, Washington, D.C., United States: American Society of Civil Engineers; 2002, p. 34–43. https://doi.org/10.1061/40650(2003)4.

[29] Haaland SE. Simple and Explicit Formulas for the Friction Factor in Turbulent Pipe Flow. Journal of Fluids Engineering 1983;105:89–90. https://doi.org/10.1115/1.3240948.

[30] Ramey HJ. Wellbore Heat Transmission. Journal of Petroleum Technology 1962;14:427–35. https://doi.org/10.2118/96-PA.

[31] Chiu K, Thakur SC. Modeling of Wellbore Heat Losses in Directional Wells Under Changing Injection Conditions. SPE Annual Technical Conference and Exhibition, Dallas, Texas: SPE; 1991, p. SPE-22870-MS. https://doi.org/10.2118/22870-MS.

[32] Pruess K. Enhanced geothermal systems (EGS) using CO2 as working fluid—A novel approach for generating renewable energy with simultaneous sequestration of carbon. Geothermics 2006;35:351–67. https://doi.org/10.1016/j.geothermics.2006.08.002.

[33] Incropera FP, DeWitt DP, Bergman TL, et al. Fundamentals Of Heat And Mass Transfer. Sixth Edition. John Wiley & Sons; 2001.

[34] Pallis P, Varvagiannis E, Braimakis K, et al. Development, experimental testing and techno-economic assessment of a fully automated marine organic rankine cycle prototype for jacket cooling water heat recovery. Energy 2021;228:120596. https://doi.org/10.1016/j.energy.2021.120596.

[35] Kaufmann F, von Zabienski J, von Ribbeck L, et al. Experimental analysis of a reversible high-temperature heat pump/ORC test rig for geothermal CHP applications. Applied Thermal Engineering 2025;280:128360. https://doi.org/10.1016/j.applthermaleng.2025.128360.